

EPJ D



Recognized by European Physical Society

Atomic, Molecular,
Optical and Plasma
Physics

Eur. Phys. J. D (2019) 73: 149

DOI: [10.1140/epjd/e2019-100048-1](https://doi.org/10.1140/epjd/e2019-100048-1)

Thermoelectricity of cold ions in optical lattices

Oleg V. Zhirov, José Lages, and Dima L. Shepelyansky



Thermoelectricity of cold ions in optical lattices

Oleg V. Zhironov^{1,2,3}, José Lages⁴, and Dima L. Shepelyansky^{5,a}

¹ Budker Institute of Nuclear Physics, 630090 Novosibirsk, Russia

² Novosibirsk State University, 630090 Novosibirsk, Russia

³ Novosibirsk State Technical University, Novosibirsk, Russia

⁴ Institut UTINAM, OSU THETA, CNRS, Université de Bourgogne Franche-Comté, Besançon, France

⁵ Laboratoire de Physique Théorique, IRSAMC, Université de Toulouse, CNRS, UPS, 31062 Toulouse, France

Received 28 January 2019 / Received in final form 15 May 2019

Published online 23 July 2019

© EDP Sciences / Società Italiana di Fisica / Springer-Verlag GmbH Germany, part of Springer Nature, 2019

Abstract. We study analytically and numerically the thermoelectric properties of cold ions placed in an optical lattice. Our results show that the transition from sliding to pinned phase takes place at a certain critical amplitude of lattice potential being similar to the Aubry transition for the Frenkel–Kontorova model. We show that this critical amplitude is proportional to the cube of ion density that allows to perform experimental realization of this system at moderate lattice amplitudes. We show that the Aubry phase is characterized by the dimensionless Seebeck coefficient about 50 and the figure of merit being around 8. We propose possible experimental investigations of such system with cold ions and argue that the experiments with electrons on liquid helium surface can also help to understand its unusual properties. The obtained results represent also a challenge for modern methods of quantum chemistry and material science.

1 Introduction

The Wigner crystal [1] has been realized with a variety of physical systems including cold ions in radio-frequency traps [2,3], electrons on a surface of liquid helium [4], quantum wires in solid state systems (see e.g. review [5]), and even dusty plasma in space [6].

The Cirac-Zoller proposal to perform quantum computations with trapped cold ions [7] pushed forward the cold ion investigations with generation of quantum entanglement, realization of main quantum gates and simple algorithms (see e.g. review [8]). In addition the quantum simulations of various physical systems with cold atoms became an independent and important research direction (see e.g. reviews [9,10]). At present the experiments with a chain of up to 100 cold ions have been reported [11].

The proposal to study the properties of Wigner crystal [1] in a periodic optical lattice with cold trapped ions in one-dimension (1D) has been introduced in [12]. The analytical and numerical studies performed there established the emergence of transition from sliding phase at weak potential amplitudes to the pinned crystal phase at high amplitudes. It was shown that this transition is the Aubry type transition [13] appearing in the Frenkel–Kontorova model of a chain of particles connected by springs and placed on a periodic substrate [14]. In fact, the properties of ionic chain can be locally described by the Chirikov

standard map [15] properties of which are directly linked with those of the Frenkel–Kontorova model. Thus the sliding phase corresponds to the integrable Kolmogorov–Arnold–Moser (KAM) curves while the pinned Aubry phase corresponds to the cantori invariant set embedded in the phase space component with dynamical chaos. The mathematical properties of such symplectic maps had been studied in great detail in the field of dynamical chaos (see [13,16,17]) and a variety of their physical application are highlighted in [15,18].

The proposal [12] attracted the interest of cold ion experimental groups [19,20] with the first signs of observation of the Aubry transition reported by Vuletic group [21] with 5 cold ions in a periodic potential followed by experiments with a larger number of ions placed in two chains with an effective periodic potential created by one chain acting on another one [22].

The physical properties of the Wigner crystal in a periodic potential are highly nontrivial and interesting. It was shown that the quantum model in the pinned phase has an exponentially large number of exponentially quasi-degenerate configurations with instanton quantum tunneling between these configurations in the vicinity of the vacuum state [12]. Thus this system represents an example of dynamical spin-glass model where the exponential quasi-degeneracy emerges not due to external disorder but due to nonlinearity and chaos of the underlying dynamical map. However, in addition to this interesting physics it has been argued [23,24] that this model captures the main

^a e-mail: dima@irsamc.ups-tlse.fr

mechanisms of friction at nanoscale so that the cold ion experiments can represent the microscopic friction emulators allowing to understand study tribology at nanoscale [25]. Also it was shown recently that in the case of an asymmetric potential there is emergence of the Wigner crystal diode current in one and two dimensions [26].

Of course, the applications of physics of Wigner crystal in a periodic potential to nanofriction are a very useful and important research direction. But in addition it has been shown that this system possesses exceptional thermoelectric properties [27]. The fundamental aspects of thermoelectricity had been analyzed in far 1957 by Ioffe [28,29]. At present the needs of efficient energy usage stimulated extensive investigations of various materials with high characteristics of thermoelectricity as reviewed in [30–34].

The thermoelectricity is characterized by the Seebeck coefficient $S = -\Delta V/\Delta T$ (or thermopower) which is expressed through a voltage difference ΔV compensated by a temperature difference ΔT . We use units with a charge $e = 1$ and the Boltzmann constant $k = 1$ so that S is dimensionless ($S = 1$ corresponds to $S \approx 88 \mu\text{V/K}$ (microvolt per Kelvin)). The thermoelectric materials are ranked by a figure of merit $ZT = S^2\sigma T/\kappa$ [28,29], where σ is the electric conductivity, T is material temperature and κ is the thermal conductivity. For an efficient usage of thermoelectricity one needs to find materials with $ZT > 3$ [30,33]. At present the highest ZT value observed in material science experiments is $ZT \approx 2.6$ [34]. It has been argued that the materials with an effective reduced dimensionality favor the high thermoelectric performance [35]. The results obtained in [27] showed that in the Aubry pinned phase it is possible to reach $ZT > 3$ and $S \gg 1$ while the KAM sliding phase has low values of ZT and S . However, in [27] only a case of relatively high charge density has been considered which requires high power lasers for a generation of high amplitude of periodic potential. In this work we consider the case of low ion density showing that in this case only a moderate potential amplitude is required to reach $ZT > 3$. Thus we expect that the experiments with cold ions in optical lattices can be used as emulators of thermoelectricity on nanoscale allowing to understand the physical mechanisms of efficient thermoelectricity.

In our opinion, the deep understanding of these mechanisms is required to select material with high thermoelectric properties. At present there are a lot of quantum physico-chemistry numerical computations of thermoelectric parameters for a variety of real materials (see e.g. [36,37]). With the advanced computational methods the band structures of electronic transport are determined taking into account all atom and electron interactions. However, after that, the conductivity is computed as for noninteracting electrons. In contrast, we argue that the interactions of charges (electrons or ions) are crucial for their thermoelectric properties of transport in a periodic potential of atomic structures. Due to these reasons we believe that the theoretical and experimental investigations of Wigner crystal transport in a periodic potential are crucial for the understanding of thermoelectricity at atomic and nanoscales.

We note that in addition to the cold ion experiments in optical lattices there are also other physical systems which can be used as a test bed for thermoelectricity at nanoscale. We consider as rather promising the electrons on liquid helium surfaces within narrow quasi-1D channels [38,39] and colloidal monolayers where the signatures of Aubry transition have been observed recently [40].

The paper is composed as follows: descriptions of model and numerical methods are given in Section 2, the dependence of the Aubry transition on charge density is determined in Section 3 by the numerical simulations and the reduction to the symplectic map and its local analysis via the Chirikov standard map, the formfactor of the ion structure in a periodic potential is considered in Section 4, the Seebeck coefficient S is determined in the KAM sliding phase and the Aubry pinned phase in Section 5, the dependence of figure of merit ZT on system parameters is established in Section 6 and the discussion of the results is given in Section 7.

2 Model description

The Hamiltonian of the chain of ion charges in a periodic potential is

$$\begin{aligned} H &= \sum_{i=1}^N \left(\frac{P_i^2}{2} + V(x_i) \right) + U_C, \\ U_C &= \sum_{i>j} \frac{1}{|x_i - x_j|}, \\ V(x_i) &= -K \cos x_i. \end{aligned} \quad (1)$$

Here x_i, P_i are conjugated coordinate and momentum of particle i , and $V(x)$ is an external periodic potential of amplitude K . The Hamiltonian is written in dimensionless units where the lattice period is $\ell = 2\pi$ and ion mass and charge are $m = e = 1$. In these atomic-type units the physical system parameters are measured in units: $r_a = \ell/2\pi$ for length, $\epsilon_a = e^2/r_a = 2\pi e^2/\ell$ for energy, $E_{adc} = \epsilon_a/er_a$ for applied static electric field, $v_a = \sqrt{\epsilon_a/m}$ for particle velocity v , $t_a = er_a\sqrt{m/\epsilon_a}$ for time t . The temperature T (or $k_B T$) is also measured in this dimensionless units, thus for $\ell = 1 \mu\text{m}$ the dimensionless temperature $T = 0.01$ corresponds to the physical temperature $T = 0.01\epsilon_a/k_B = 0.02\pi e^2/(\ell k_B) \approx 1 \text{ K}$ (Kelvin).

We note that in this work we consider only the problem of classical charges. Indeed, as shown in [12] the dimensionless Planck constant of the system is $\hbar_{\text{eff}} = \hbar/(e\sqrt{m\ell/2\pi})$. For a typical lattice period $\ell \approx 1 \mu\text{m}$, $\nu \sim 1$ and $^{40}\text{Ca}^+$ we have $\hbar_{\text{eff}} \approx 10^{-5}$. For electrons on a periodic potential of liquid helium with the same period $\ell \approx 1 \mu\text{m}$ we have $\hbar_{\text{eff}} \approx 2 \times 10^{-3}$. Due to this reason we consider below only the classical dynamics of charges.

Following [27] we model the dynamics of ions in the frame of Langevin approach (see e.g. [41]) with the equation of motion being

$$\dot{P}_i = \dot{v}_i = -\partial H/\partial x_i + E_{dc} - \eta P_i + g\xi_i(t), \quad \dot{x}_i = P_i = v_i. \quad (2)$$

The parameter η describes phenomenologically the dissipative relaxation processes, and the amplitude of Langevin force g is given by the fluctuation-dissipation theorem $g = \sqrt{2\eta T}$. We also use particle velocities $v_i = P_i$ (since mass is unity). The normally distributed random variables ξ_i are defined by correlators $\langle\langle \xi_i(t) \rangle\rangle = 0$, $\langle\langle \xi_i(t)\xi_j(t') \rangle\rangle = \delta_{ij}\delta(t-t')$. The amplitude of the static force is given by E_{dc} . Equations (2) are solved numerically by the 4th order Runge–Kutta integration with a time step Δt , at each such a step the Langevin contribution is taken into account, As in [27] we usually use $\Delta t = 0.02$ and $\eta = 0.02$ with the results being not sensitive to these parameters.

The length of the system in 1D case is taken to be $2\pi L$ in x -direction with L being the integer number of periods with periodic or hard-wall boundary conditions for N ions inside the system. The dimensionless charge density is $\nu = N/L$ being related to the winding number of the KAM curves in the related symplectic map description of equilibrium positions of ions.

We note that the Langevin description of a system evolution is a standard approach for analysis of the system when it has a fixed temperature created by the contact with the thermal bath or certain thermostat. The origin of this thermostat is not important since this description is universal [41]. For experiments with cold ions we assume that the thermostat is created by external environment, residual gas etc. For the computation of the Seebeck coefficient we need to have a temperature gradient along the ion chain. In the frame of the Langevin equation this is realized easily simply by imposing in (2) that T is a function of the ion position along the chain with $T = T(x) = T_0 + gx$ where T_0 is the average temperature along the chain and $g = dT/dx$ is a small temperature gradient (here x is a coordinate position of a given ion). In the experiments with cold ions such a temperature gradient can be created by multiple laser beams which generate a fluctuating force $f(x)$. The average force should be zero while its square $f^2(x)$ should change linearly along the chain. These fluctuating forces of laser beams will create additional ion velocity fluctuations with $(\delta v_i)^2 \propto f^2(x) \propto (T(x) - T_0) = gx$ thus producing a temperature gradient along the ion chain. We return to the discussion of the thermalization in experiments later.

For clarity we note that the results of Sections 3 and 4 are obtained with interactions between all ions, while the results obtained with the Langevin dynamics presented in Sections 5 and 6 are obtained with nearest neighbor interactions between ions (in [27] it was shown that this approximation still provides a good description of the case of all interacting ions).

3 Density dependence of the Aubry transition

The equilibrium static positions of ions in a periodic potential are determined by the conditions $\partial H/\partial x_i = 0$, $P_i = 0$ [12,13]. In the approximation of nearest neighbor interacting ions, this leads to the symplectic map for recurrent ion positions x_i

$$p_{i+1} = p_i + Kg(x_i), \quad x_{i+1} = x_i + 1/\sqrt{p_{i+1}}, \quad (3)$$

where the effective momentum conjugated to x_i is $p_i = 1/(x_i - x_{i-1})^2$ and the kick function $Kg(x_i) = -dV/dx|_{x=x_i} = -K \sin x_i$. Below we show that this map with only nearest neighbor interacting ions provides a good description of the case of interactions between all ions.

The map (3) can be locally (in the phase space) described by the Chirikov standard map. This procedure is standard and is described in [15,16]. With this aim the second equation in (3) for ion positions x_{i+1} is locally linearized in p_{i+1} near the resonant values of $p_r(m) = 1/(2\pi m)^2 \approx (\nu/2\pi)^2$ defined by the condition $x_{i+1} = x_i + 2\pi m \approx x_i + 2\pi/\nu$ where m are integers. This leads to the local description of dynamics by the Chirikov standard map [12,15]:

$$y_{i+1} = y_i - K_{\text{eff}} \sin x_i, \quad x_{i+1} = x_i - y_{i+1}, \quad (4)$$

where $y_i = \alpha(p_i - p_r)$, $\alpha = 1/(2p_r^{3/2}) = (2\pi/\nu)^{3/2}/2$ and the dimensionless chaos parameter $K_{\text{eff}} = \alpha K = K(2\pi/\nu)^3/2$. As it is shown in [15–17] the global chaos border is determined by the critical $K_{\text{eff}} \approx 1$.

As in [12] the validity of the map description is checked numerically finding the ground state configuration using numerical methods of energy minimization described in [12,13]. In these simulations the Coulomb interactions between all ions are considered. Also we use the hard-wall boundary conditions at the ends of ion chain assuming that in the experiments it can be created by specific laser frequency detuning from resonant transition between ion energy levels. Due to these boundary conditions the smoothed ion density is inhomogeneous since an ion near boundary vicinity has more pressure from other ions in the chain (a similar inhomogeneous density appears for ions inside a global oscillator potential of a trap as discussed in [12]). To avoid the non-homogeneity of the average local density (see Fig. 1, where we see that this density increases near the chain ends) we select the central part of the chain with approximately 1/3 of all ions where the average local density is approximately constant (we distinguish average local density from the local density as defined in Fig. 1 caption). The examples of ion density for KAM sliding and Aubry pinned phases are shown in Figure 1. The data show that the local distribution of ions is relatively smooth in the sliding phase and is rather peaked in the pinned phase. The selected density is chosen to be close to the inverse of the golden mean value $\nu = \tilde{\nu}_g = \nu_g^{-1} = \nu_g - 1 = (\sqrt{5} - 1)/2 = 0.618\dots$ which is often used for stability analysis of KAM curves in symplectic maps (see e.g. [16,17]). With the choice $N/L = 55/89$, typical for common Frenkel–Kontorova model as a rational approximant to the golden mean, we have actually $\nu = 0.56$, and we need to adjust the number of ions N in order to approach the required value $\tilde{\nu}_g = 0.618\dots$

We note that this problem of local density change disappears if one restricts himself by the account for the nearest neighbors interactions between ions: in this approach the ion density becomes practically constant along the whole chain. This approach is used below in our simulations of kinetic properties of the system.

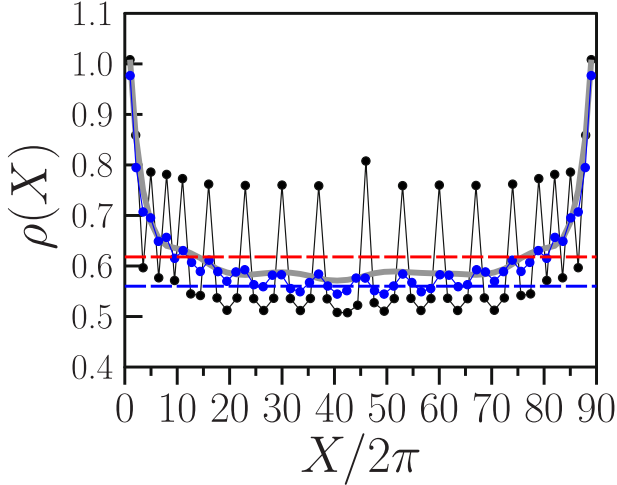


Fig. 1. Local ion density distribution is shown along the ion chain for the sliding phase at $K = 0.001$ (blue points connected by lines) and for the pinned phase at $K = 0.01$ (black points connected by lines). Here the local density is defined as $\rho(X) = 2\pi/(x_{i+1} - x_i)$ and $X = (x_{i+1} + x_i)/2$; the gray curve shows the average local density distribution obtained from averaging of local density over approximately 5 ions. The red dashed line corresponds to the fraction of golden mean density $\rho(X) = \nu_g - 1 = (\sqrt{5} - 1)/2 = 0.618\dots$, and the blue dashed line corresponds to $\rho(X) = \nu = 0.56$ obtained from the formfactor data (see Fig. 6 below). Here the ratio of N and L is $N/L = 55/89 \approx \nu_g \approx 0.618\dots$

The analysis of ground state stationary positions of ions in a periodic potential is shown in Figure 2 for the KAM sliding phase ($K = 0.001$) and the Aubry pinned phase ($K = 0.01$) at $N/L = 60/89$ ratio which gives approximately the golden mean fraction $\nu \approx \tilde{\nu}_g \approx 0.618$ in the middle part of the chain. Even if the Coulomb interactions between all ions are considered the kick function $g(x)$ is close to the theoretical one $g(x) = -\sin x$. This shows that the approximation of nearest neighbors used in the symplectic map (3) gives us a good approximation of the system. For $K = 0.001$ the positions of ions follow the invariant KAM curve while for $K = 0.01$ the ion positions form an invariant Cantor set (cantori) appearing on the place of destroyed KAM curve. The hull function is defined as $h(x) = (x_i + \pi)[\text{mod } 2\pi] - \pi$ with $x = (2\pi(i-1)/\nu - \pi/2)[\text{mod } 2\pi] - \pi$, where $i \in (N/3, \dots, 2N/3)$. This function expresses the actual ion positions in presence of the periodic potential as the function of ion positions in absence of this potential. Indeed, at $K \rightarrow 0$ we have $h(x) = x$ with a smooth deformation for small perturbations while in the pinned phase we obtain the devil's staircase corresponding to the fractal cantori structure. This is the standard method used for the description of the invariant KAM curves and fractal cantori when the KAM curve is destroyed (see more detail in [13,16,17]). The transition from the smooth hull function to the devil's staircase is visible in the data of Figure 2 even if there is a certain spreading of points especially in the KAM phase which we attribute to a rather small value of $K = 0.001$. Thus the obtained data show that with

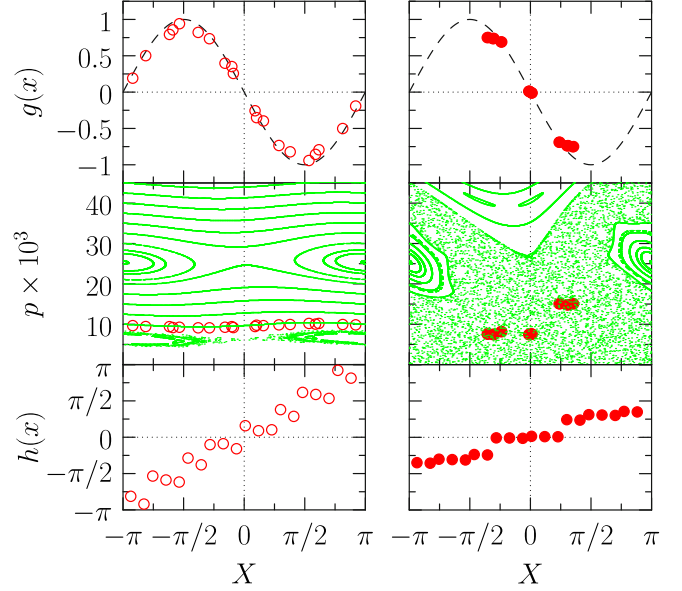


Fig. 2. Functions related to the dynamical map obtained from the ground state equilibrium positions x_i of ions at $K = 0.001$ (open circles, left column) and $K = 0.01$ (full circles, right column). Panels show: the kick function $g(x)$ (top); the phase space (p, x) of the map with $g(x) = -\sin x$ (green/light-gray points) and actual ion positions (red/circles) (middle); the hull function $h(x)$ (bottom). The ion positions are shown via the hull function $h(x) = (x_i + \pi)[\text{mod } 2\pi] - \pi$ versus $x = (2\pi(i-1)/\nu - \pi/2)[\text{mod } 2\pi] - \pi$, for the central 1/3 part of the chain; $i \in (N/3, \dots, 2N/3)$. Here $N/L = 60/89$.

$\nu \approx 0.618$ the Aubry transition takes place at a certain $K_c(\nu)$ inside the interval $0.001 < K_c(\nu) < 0.01$.

It is important to note that a similar approximate symplectic map description for static charge positions is working well not only in the case of periodic potential but also for wiggling channel structures analyzed in [42].

To obtain the critical amplitude in a more exact way we determine the static ion configuration at a fixed density $\nu = N/L$ and then compute the phonon spectrum $\omega(k)$ of small ion oscillations near the equilibrium positions. Such an approach was already used and described in [12,13]. An example of the photon spectrum $\omega(k)$ is shown in Figure 3 for $N/L = 55/89$. Below the transition at $K < K_c(\nu)$ we have the linear acoustic type spectrum $\omega \approx C_v k$ of phonon type excitations describing ion oscillations near their static equilibrium positions like those shown in Figure 2 at $N/L = 60/89$. Here, $k = i/N$ plays the role of the wave vector and $C_v \approx 0.2$ is the sound velocity. The lowest phonon frequency goes to zero with the increase of the system size as $\omega(k = 1/N) \approx C_v/N$. The spectrum becomes drastically different above the transition $K > K_c(\nu)$ with appearance of the optical gap ω_0 in the spectrum $\omega(k)$. In fact, the gap ω_0 is proportional to the Lyapunov exponent of symplectic map orbits located on the corresponding fractal cantori set [13,16]. It is independent of the system size N .

In principle, it is possible to search numerically for the value of $K_c(\nu)$ at which a nonzero optical gap appears in

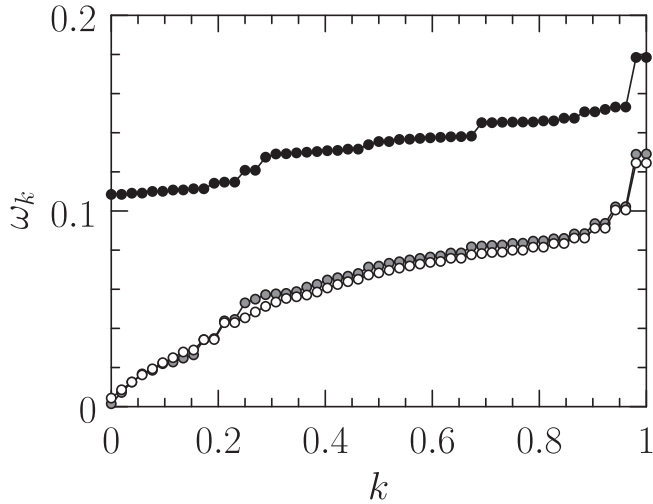


Fig. 3. Spectrum of phonon excitations $\omega(k)$ as a function of scaled mode number $k = i/N$ ($i = 1, \dots, N-2$), for $K = 0.001$ (bottom curve, open circles), $K = 0.002$ (bottom curve, gray circles) and $K = 0.015$ (top curve, full circles). Here there are $N = 55$ ions and $L = 89$ lattice periods.

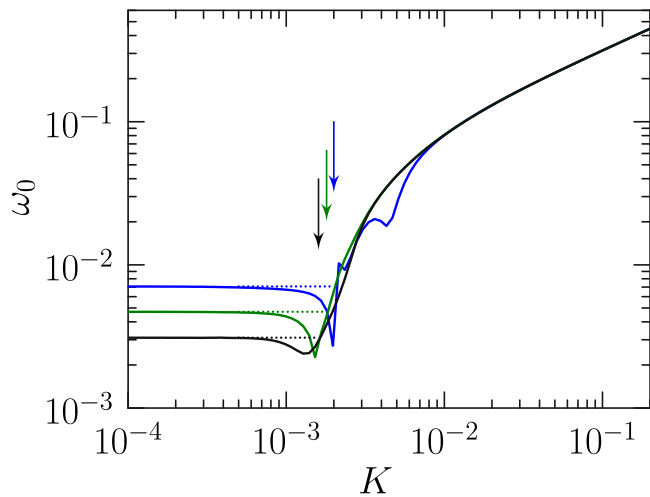


Fig. 4. The lowest mode phonon frequency $\omega_0(K)$ vs the periodic potential coupling K . Blue, green and black curves correspond to $N/L = 34/55, 55/89$ and $89/144$. The position of the Aubry transition $K = K_c$ indicated by arrow is defined as an intersection of the curve $\omega_0(K)$ with the level shown by the dotted line at $\omega_0(K = 0)$. Three arrows correspond to different winding numbers (densities) $\nu = 34/55, 55/89$ and $89/144$ and correspond to $K_c = 0.002, 0.0018$ and 0.0016 .

the spectrum $\omega(k)$. However, we find more useful to compute the dependence of lowest frequency $\omega_0 = \omega(k = 1/N)$ on the amplitude K . In the KAM phase we have $\omega_0(K)$ being independent of K and thus we determine the critical $K_c(\nu)$ by the intersection of horizontal line $\omega_0(K) = \omega_0(K = 0)$ with the curve of the spectrum $\omega_0(K)$ at higher K values ($\omega_0(K = 0) = \omega_0(K)$). The example of this intersection procedure is shown in Figure 4 at increasing Fibonacci approximates $N/L = 34/55, 55/89, 89/144$. We estimate the accuracy of this method of K_c computation

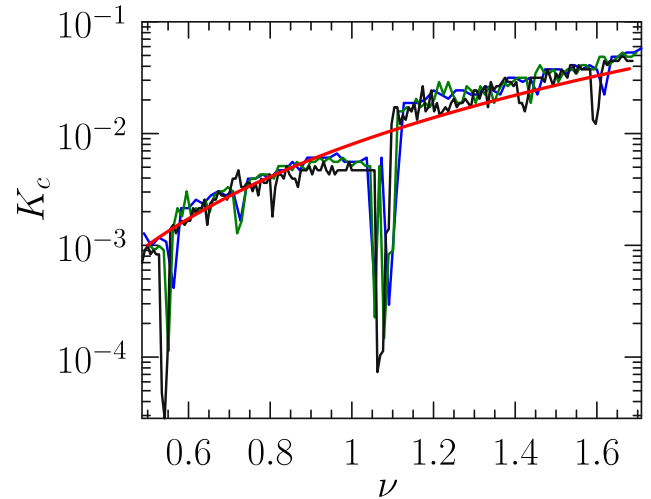


Fig. 5. Dependence of the critical coupling K_c on the winding number $\nu = N/L$. Blue, green and black curves correspond to $L = 55, 89$ and 144 ; for each L the number of ions N takes all integer values up to corresponding highest/lowest ν value. The red curve corresponds to theoretical estimate: $K_c = 0.034(\nu/1.618)^3$.

on the level of 10%–15% of K_c value. At small sizes like $34/55$ a wiggling of curve at higher K decreases the accuracy. But at longer sizes the result is stable. Thus we obtain the critical $K_c(\nu) \approx 0.0017$ for the irrational density $N/L = \nu = \nu_g = 0.618\dots$, taking the average value for sizes $55/89$ and $89/144$.

The numerically obtained dependence of the critical amplitude of Aubry transition $K_c(\nu)$ on ion density ν is shown in Figure 5 for the range $0.5 \leq \nu \leq 1.7$. The numerical values $K_c(\nu)$ are obtained as in Figure 4 for the lattice size $L = 55, 89, 144$ and for all integer N values appearing inside the interval $0.5 \leq \nu \leq 1.7$. On average the numerical values are in a good agreement with the theoretical expression given in [12]

$$K_c(\nu) \approx 0.034(\nu/\nu_g)^3, \quad \nu_g = 1.618\dots \quad (5)$$

This formula is obtained on the basis of local reduction of map (3) to the Chirikov standard map with a homogeneous density of nonlinear resonances. For that the second equation (3) is linearized near $1/\sqrt{p} = 2\pi/\nu_g$ that gives the Chirikov standard map with chaos parameter $K_{\text{eff}} = K(2\pi/\nu_g)^3/2$ and the critical value $K_c = 0.034$ at $\nu_g = 1.618\dots$ corresponding to $K_{\text{eff}} \approx 1$. Indeed, the KAM curve with a given ν is destroyed when the global chaos appears in the Chirikov standard map (4) at $K_{\text{eff}} = K_c(\nu)(2\pi/\nu)^3/2 \approx 1$ that leads to the dependence (5). More details of this method are given in [12,15,16,43]. For $\nu = \nu_g = 1.618\dots$, the detailed numerical analysis gives $K_c(\nu) \approx 0.0462$ [12,27] (instead of 0.034) and for $\nu = 0.618\dots$ we have $K_c(\nu) \approx 0.0017$ (instead of 0.0189). The strongest deviations from the theoretical dependence (5) take place at $\nu \approx 0.55$ and $\nu \approx 1.06$ with a significant drop of K_c . In fact, these ν values are located in the vicinity of main resonances with $\nu = 1/2; 1$ which are slightly shifted from their rational positions due to

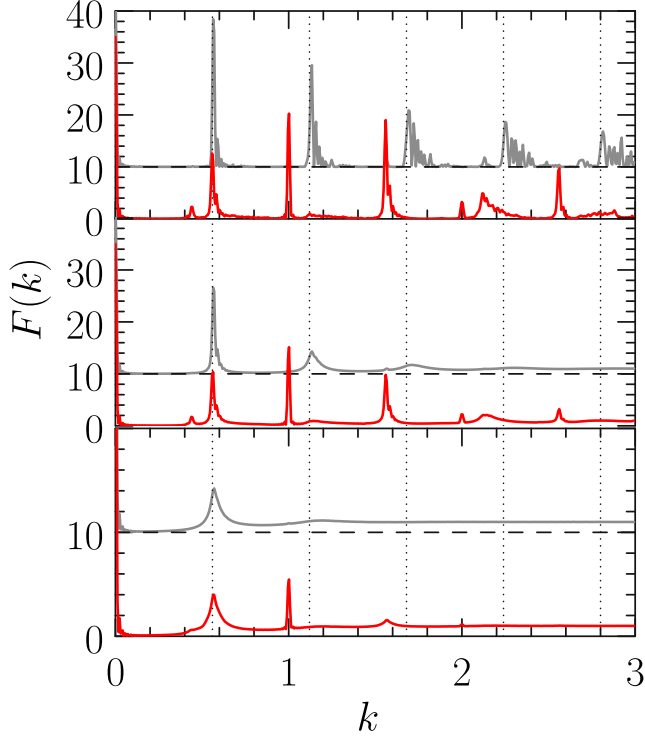


Fig. 6. Dependence of the formfactor $F(k)$ on k below the Aubry transition ($K = 0.001 < K_c = 0.00189$) (KAM sliding phase, gray curves) and above ($K = 0.01 > K_c = 0.002$) (pinned mode, red curves). For a clarity the gray curves are shifted up by 10. The temperature takes values $T = 10^{-6}, 2 \times 10^{-3}, 10^{-2}$ for top, middle and bottom panels respectively. Here $N/L = 55/89$. Dotted curves indicate the peak positions at $k_i = \nu i$, where $\nu = 0.56$ is the mean rotation number at the central region of the chain. (compare this value of ν to that in the Fig. 1). The formfactor is calculated over central part of ion chain, contributions from 10 ions from each edge are ignored.

inhomogeneity of ion density appearing due to the hard-wall boundary conditions (see Fig. 1). In a vicinity of rational resonances there is a stochastic layer inside which the dynamical chaos emerges at rather small critical perturbations (see [15,16]).

In the following the analysis of the thermodynamic characteristics is done for $\nu \approx 0.618$. In the related Figures 7–11 for rescaling of parameters to the dimensionless units we use $K_c = 0.002$ which is close to the theoretical value $K = 0.00189$ from (5).

Thus in global the numerical results obtained here for the dependence $K_c(\nu)$ on density are in good agreement with the theory (5) developed in [12]. The most striking feature of this dependence is the sharp decrease of K_c with ν . This allows to observe the Aubry transition at significantly smaller laser powers simply by a moderate decrease of density ν (see discussion below).

4 Formfactor of the ion structure

It is useful to characterize the structure of ions in a periodic potential by the formfactor $F(k)$ given by

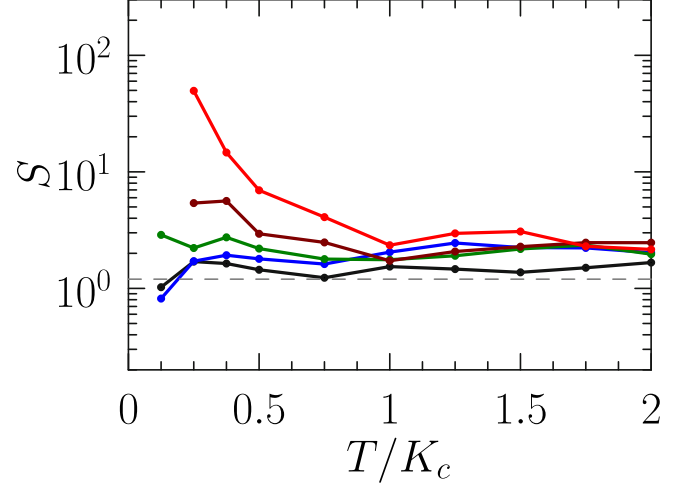


Fig. 7. Dependence of Seebeck coefficient S on temperature T at different values $K/K_c = 0$ (black), 1 (blue), 2 (green), 3 (brown), 4 (red). Here the ratio of number of N ions to number of lattice periods L is $N/L = 21/34$ and $K_c = 2 \times 10^{-3}$. Dashed line shows $S = 1.2$ value at $K = 0$ for noninteracting particles.

$$F(k) = \left\langle \left| \sum_{i \neq j}^{N_{cr}} \exp(ik(x_i(t) - x_j(t))) \right|^2 \right\rangle / N_{cr}, \quad (6)$$

where the sum is taken by the central part of the chain with approximately $N_{cr} \approx N/3$. The positions of ions $x_i(t)$ at different moments of time are obtained at finite temperature T with the Langevin equations (2) with averaging over time. Here we use the hard-wall boundary conditions and Coulomb interactions act between all electrons ions. Here we use the Metropolis algorithm for simulation of the thermal effects (see e.g. [12,42]), rather than the Langevin equation, and the nearest neighbor approximation is not necessary.

The variation of $F(k)$ with temperature is shown in Figure 6 for the KAM sliding phase and the Aubry pinned phase. In the KAM phase at $K < K_c$ the peaks of $F(k)$ are located at $k \approx i\nu$ corresponding to integer harmonics i of average ion density $\nu \approx 0.56$ in the central part of the chain. In contrast, in the Aubry phase at $K > K_c$ there appear additional integer peaks at $k \approx i$ being commensurate with the lattice period. At low temperature $T = 10^{-6}$ the peaks of $F(k)$ are well visible and clearly demonstrate the transition from incommensurate phase at $K < K_c$ to the quasi-commensurate phase above the Aubry transition at $K > K_c$. with the increase of temperature the high harmonics in $F(k)$ are washed out by thermal fluctuations. We think that the analysis of formfactor structure can be rather useful for experimental investigations of Aubry transition.

5 Seebeck coefficient

The computations of the Seebeck coefficient S are done in the frame of Langevin equations (2) with the hard-wall boundary conditions. We note that in the Aubry

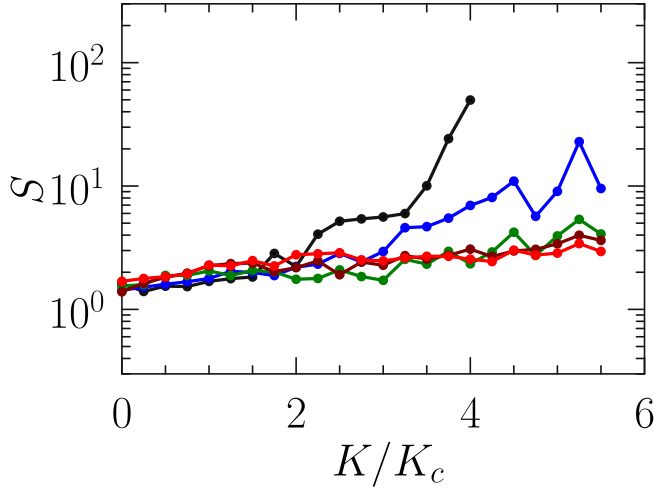


Fig. 8. Seebeck dependence on K at different temperatures $T/K_c = 0.25$ (black), 0.5 (blue), 1 (green), 1.5 (cyan), 2 (red). Here the ratio of number of N ions to number of lattice periods L is $N/L = 21/34$ and $K_c = 2 \times 10^{-3}$.

pinned phase long computational times are required. This is due to the fact that ion pinned in one well of the periodic potential have a small probability $\propto \exp(-B/T)$ of thermal fluctuations to overcome the barrier of a height $B \sim (K - K_c)$. Thus we made simulations with times up to $t = 10^8$. In physical units this corresponds to $t \sim 10^8 t_a \sim 10^{-2}$ s, for $\ell \sim 1 \mu\text{m}$ and ions $^{40}\text{Ca}^+$, while ions can now be trapped for hours [11]. In these simulations for each ion we take into account the Coulomb interactions only with nearest left and right neighbor ions that allow to accelerate the computations. As in [27] we ensured that the obtained results are not sensitive to inclusion of interactions with other neighbors.

The computations of S are done with the procedure developed in [27]. At fixed temperature T we apply a static field E_{dc} which creates a voltage drop $\Delta V = E_{dc} 2\pi L$ and a gradient of ion density $\nu(x)$ along the chain. Then at $E_{dc} = 0$ within the Langevin equations (2) we impose a linear gradient of temperature ΔT along the chain and in the stabilized steady-state regime determine the charge density gradient of $\nu(x)$ along the chain (see e.g. Fig. 2 in [27]). The data are obtained in the linear regime of relatively small E_{dc} and ΔT values. Then the Seebeck coefficient is computed as $S = \Delta V / \Delta T$ where ΔV and ΔT are taken at such values that the density gradient from ΔV compensates the one from ΔT .

The dependencies of S on temperature T at different amplitudes K of the periodic potential are shown in Figure 7. In the KAM sliding phase with $K \leq K_c$ there is no significant change of $S \approx 2$, which remains close to its value $S = 1.2$ for free noninteracting particles. In contrast in the Aubry pinned phase with $K/K_c > 1$ we obtain an exponential increase of S at $T/K_c < 0.5$. This increase of S is especially visible for $K/K_c = 4$ where the maximal reached value is $S \approx 50$.

We note that a similar strong growth of S at low temperatures has been reported in experiments with quasi-one-dimensional conductor $(\text{TMTSF})_2\text{PF}_6$ [44] where as

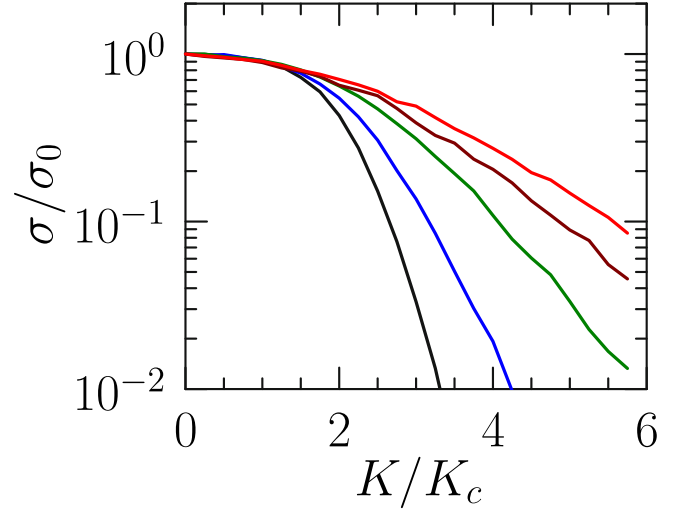


Fig. 9. Dependence of conductivity on K at different temperatures $T/K_c = 0.25$ (black), 0.5 (blue), 1 (green), 1.5 (brown), 2 (red). Here the ratio of number of N ions to number of lattice periods L is $N/L = 21/34$, $\eta = 0.02$, $\sigma_0 = \nu / (2\pi\eta)$ with $\nu = 0.618$ and $K_c = 2 \times 10^{-3}$.

high as $S = 400$ value had been reached at low temperatures (see Fig. 3 in [44]).

The dependence of S on K is shown in Figure 8. At low temperatures $T < K_c$ there is a sharp increase of S with increase of $K > K_c$ with a maximal reached value $S \approx 60$. In a certain sense the increase of K drives the system deeper and deeper into the insulating phase with larger and larger resistivity. Thus we can say that S increases with the increase of sample resistivity. A similar dependence has been observed in experiments with two-dimensional electron gas in highly resistive (pinned) samples of micron size (see Fig. 8 in [45]).

Thus we can say that our numerical results are in a qualitative agreement with the experiments [44,45].

6 Figure of merit ZT

To determine the figure of merit ZT we need to compute in addition to S the electrical conductivity σ and the heat conductivity κ . The computation of σ is done by applying a weak E_{dc} field acting on a circle with periodic boundary conditions. Then we compute the ion velocity v_{ion} averaged over all particles and time interval. Then the charge current is $j = \nu v_{\text{ion}} / 2\pi$ and $\sigma = j / E_{dc}$. At $K = 0$ the ion crystal moves as a whole with $v_{\text{ion}} = E_{dc} / \eta$ corresponding to the conductivity of free particles $\sigma = \sigma_0 = \nu / (2\pi\eta)$ that is confirmed by numerical simulations (see Fig. 9).

The dependence of σ on K and temperature T is shown in Figure 9. In the KAM sliding phase at $K < K_c$, σ / σ_0 is practically independent of T and K . However, in the Aubry pinned phase at $K > K_c$ there is an exponential drop of σ / σ_0 with increase of K and with decrease of T .

For the computation of heat conductivity κ we use the approach developed in [27]. The heat flow J is related to the temperature gradient by the Fourier law with the

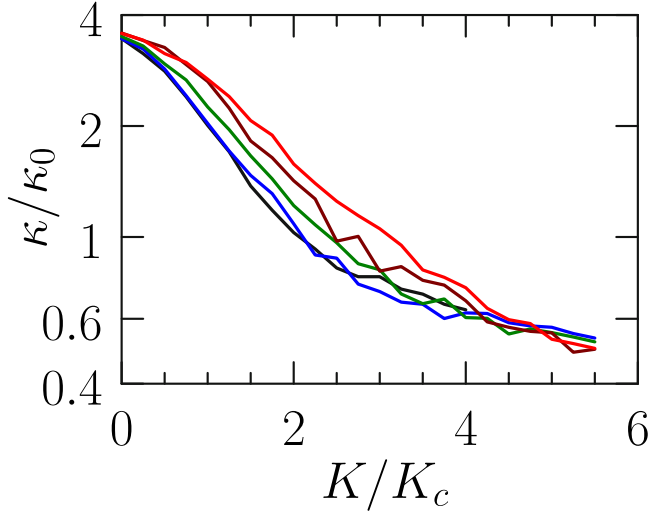


Fig. 10. Dependence of heat conductivity κ on K at different temperatures $T/K_c = 0.25$ (black), 0.5 (blue), 1 (green), 1.5 (brown), 2 (red). Here the ratio of number of N ions to number of lattice periods L is $N/L = 21/34$, $\eta = 0.02$, $\kappa_0 = \sigma_0 K_c$ and $K_c = 2 \times 10^{-3}$.

thermal conductivity κ : $J = \kappa \partial T / \partial x$ [31,41]. The heat flow is computed from forces acting on a given ion i from left and right sides being respectively $f_i^L = \sum_{j < i} 1/|x_i - x_j|^2$, $f_i^R = -\sum_{j > i} 1/|x_i - x_j|^2$. For an ion moving with a velocity v_i these forces create left and right energy flows $J_{L,R} = \langle f_i^{L,R} v_i \rangle_t$. In a steady state the mean ion energy is independent of time and $J_L + J_R = 0$. But the difference of these flows gives the heat flow along the chain: $J = (J_R - J_L)/2 = \langle (f_i^R - f_i^L) v_i / 2 \rangle_t$. We perform such computations of the heat flow, with hard wall boundary conditions. In addition to the method used in [27] we perform time averaging using accurate numerical integration along the ions trajectories that cancels contribution of large oscillations due to periodical motion of ions. In this way we determine the thermal conductivity via the relation $\kappa = JL/\Delta T$. The obtained results for κ are independent of small ΔT . Our previous result confirm that the thermodynamic characteristic are independent of system size [27].

The dependence of heat conductivity κ on K and T is shown in Figure 10. For convenience we present the ratio of κ to $\kappa_0 = \sigma_0 K_c$ to have the results in dimensionless units. There is an exponential decrease of κ/κ_0 with increase of $K > K_c$ showing that for ionic phonons the propagation along the chain becomes more difficult at high K amplitudes. The decrease of T leads to a decrease of κ/κ_0 but this drop is less pronounced comparing to those for σ/σ_0 .

From the obtained values of S , σ and κ at $\nu \approx 0.618$ we compute the figure of merit ZT shown in Figure 11 as a function of K/K_c at different temperatures. At fixed T there is an optimal maximal ZT value located approximately at $K/K_c \approx 2.5$ while at smaller and higher K/K_c values we have a decrease of ZT . The maximal ZT value increases with the growth of temperature and the width of the peak becomes broader. At the maximum with $T/K_c = 2$ and $K/K_c = 2.5$ we obtain $ZT \approx 8$. This

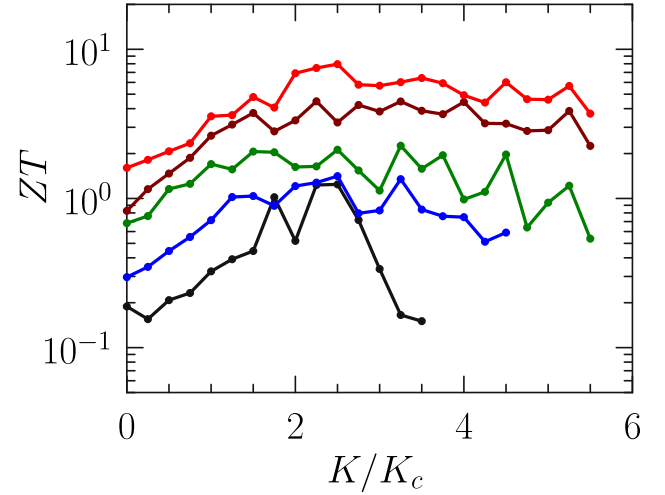


Fig. 11. Dependence of figure of merit ZT on K at different temperatures $T/K_c = 0.25$ (black), 0.5 (blue), 1 (green), 1.5 (brown), 2 (red). Here the ratio of number of N ions to number of lattice periods L is $N/L = 21/34$, $\eta = 0.02$ and $K_c = 2 \times 10^{-3}$.

maximal ZT value is by factor 2 larger than the value obtained at $\nu \approx 1.618$, $T/K_c \approx 3$ and $K/K_c \approx 3.5$ in [27]. We suppose that a more dilute ion density favors more efficient thermodynamical characteristics.

The presented data in general demonstrate a growth of ZT with increase of temperature T . This trend is in a qualitative agreement with the experimental results in material science [33,34]. However, very high temperatures are not of significant interest when they become much higher than room temperature. For our model it is clear that for $T \gg K$ we go to the limit of ion chain in absence of periodic potential with an effective sliding regime with $S \approx 1$ and small ZT . There are signs of drop of ZT at high T visible in [27] (Figs.5,7 there). However, the region of very high T corresponds to high ion velocities thus requiring smaller integration step and longer CPU times.

Our studies are done for the strictly 1D case. It is important to consider extensions to the two-dimensional (2D) case which may be useful for electrons on liquid helium and material science. Indeed, in quasi-1D case it is known that transfer dynamics can lead to excitation of transfer modes and zigzag instabilities [46,47]. However, the recent results reported for 2D Wigner crystal transport indicate that there is similarity between 1D and 2D properties and thus we expect that the obtained results will be useful for higher-dimensional systems.

7 Discussion

In this work we analyzed the properties of cold ion chain placed in a periodic potential. The results show the emergence of Aubry transition from KAM sliding phase to Aubry pinned phase when the amplitude of the potential exceeds a critical value $V_A = K_c(\nu)e^2/(\ell/2\pi)$. For a typical period of optical lattice $\ell = 1 \mu m$ and dimensionless ion

density per period $\nu = 1.618$, with $K_c \approx 0.034$, this corresponds to $V_A \approx 3$ K (Kelvin) that would require rather strong laser power for creation of such optical potential. However, with a decrease of ν we have a cubic drop of V_A and thus for $\nu = 0.38$ we need only $V_A \approx 0.04$ K that is much more accessible for optical lattice experiments.

The interest of the Aubry phase is related to high thermodynamic properties appearing in this phase. Thus we show that one can reach in this phase the high values of Seebeck coefficient $S \approx 50k_B/e \approx 4400 \mu\text{V/K}$ which approaches to the record experimental values $S \approx 400 k_B/e$ observed in quasi-one-dimensional materials [44] and with two-dimensional electron gas in small disordered samples with $S \sim 50 k_B/e$ [45]. Even more remarkable is that in this phase the figure of merit can be as such high as $ZT \approx 8$ being above the record experimental values [34]. We suppose that for cold ions in optical lattices the voltage difference δV can be easily created by a weak external static electric field while the temperature difference ΔT at the ends of the lattice can be generated by additional laser beams heating generating a small change of temperature along the ion chain. We note that there is now a significant progress with the temperature control of cold ions and atoms (see e.g. [48–50]) that allows to hope on experimental generation of temperature gradients for Seebeck coefficient measurements in near future. Thus such experiments would allow to investigate the thermodynamical properties of Wigner crystal of cold ions in optical lattice. We assume that the investigations of thermoelectric properties with cold ions in optical lattices may bring us to a deep understanding of thermoelectricity which will be further used for selection of optimal thermoelectric materials.

Also we think that the simple models considered here raise an important challenge for computational methods of quantum chemistry where interactions of electrons and atoms are taking into account in the computations of band structures but after that the thermoelectric characteristics are computed for effectively noninteracting electrons (see e.g. [36,37]). We argue that our results clearly show that the high thermoelectric characteristics appear only in the Aubry pinned phase where the interactions between charges play a crucial role. We argue that our results challenge the further development of methods of quantum chemistry.

Thus the above analysis clearly demonstrates the importance of Aubry pinned phase for high thermoelectric performance. Due to that the experimental investigations of the Aubry transition with cold ions in optical lattices and electrons on liquid helium will bring to us important fundamental results useful for development of efficient thermoelectric materials.

This work was supported in part by the Programme Investissements d’Avenir ANR-11-IDEX-0002-02, reference ANR-10-LABX-0037-NEXT (project THETRACOM); it was granted access to the HPC resources of CALMIP (Toulouse) under the allocation 2017-P0110. This work was also supported in part by the Programme Investissements d’Avenir ANR-15-IDEX-0003, ISITE-BFC (project GNETWORKS), and in part by the

Bourgogne Franche-Comté Region 2017-2020 APEX Project. For OVZ this work is partially supported by the Ministry of Education and Science of the Russian Federation. One of us (DLS) thanks R.V. Belosludov and V.R. Belosludov for discussions of methods of quantum chemistry used for computations of thermoelectric characteristics in real materials.

Author contribution statement

All authors equally contributed to all stages of this work.

References

1. E. Wigner, Phys. Rev. **46**, 1002 (1934)
2. G. Birkl, S. Kassner, H. Walther, Nature **357**, 310 (1992)
3. D.H.E. Dubin, T.M. O’Neil, Rev. Mod. Phys. **71**, 87 (1999)
4. Y. Monarkha, K. Kono, *Two-Dimensional Coulomb Liquids and Solids* (Springer-Verlag, Berlin, 2004)
5. J.S. Meyer, K.A. Matveev, J. Phys.: Condens. Matter **21**, 023203 (2009)
6. V.E. Fortov, A.V. Ivlev, S.A. Khrapak, A.G. Khrapak, G.E. Morfill, Phys. Rep. **421**, 1 (2005)
7. J.I. Cirac, P. Zoller, Phys. Rev. Lett. **74**, 4091 (1995)
8. R. Blatt, D. Wineland, Nature **453**, 1008 (2008)
9. M. Johanning, A.F. Varon, C. Wunderlich, J. Phys. B: At., Mol. Opt. Phys. **42**, 154009 (2009)
10. R. Blatt, C.F. Roos, Nat. Phys. **8**, 277 (2012)
11. G. Pagano, P.W. Hess, H.B. Kaplan, W.L. Tan, P. Richerme, P. Becker, A. Kyprianidis, J. Zhang, E. Birkelbaw, M.R. Hernandez, Y. Wu, C. Monroe, [arXiv:1802.03118](https://arxiv.org/abs/1802.03118) (2018)
12. I. Garcia-Mata, O.V. Zhirov, D.L. Shepelyansky, Eur. Phys. J. D **41**, 325 (2007)
13. S. Aubry, Physica D **7**, 240 (1983)
14. O.M. Braun, Yu.S. Kivshar, *The Frenkel–Kontorova Model: Concepts, Methods, Applications* (Springer-Verlag, Berlin, 2004)
15. B.V. Chirikov, Phys. Rep. **52**, 263 (1979)
16. A.J. Lichtenberg, M.A. Leiberman, *Regular and Chaotic Dynamics* (Springer, Berlin, 1992)
17. J.D. Meiss, Rev. Mod. Phys. **64**, 795 (1992)
18. B. Chirikov, D. Shepelyansky, Scholarpedia **3**, 3550 (2008)
19. T. Pruttivarasin, M. Ramm, I. Talukdar, A. Kreuter, H. Haffner, New J. Phys. **13**, 075012 (2011)
20. A. Bylinskii, D. Gangloff, V. Vuletic, Science **348**, 1115 (2015)
21. A. Bylinskii, D. Gangloff, I. Countis, V. Vuletic, Nat. Mater. **15**, 717 (2016)
22. J. Kiethe, R. Nigmatullin, D. Kalincev, T. Schmirander, T.E. Mehlstaubler, Nat. Commun. **8**, 15364 (2017)
23. A. Benassi, A. Vanossi, E. Tosatti, Nature Commun. **2**, 236 (2011)
24. D. Mandelli, E. Tosatti, Nature **526**, 332 (2015)
25. N. Manini, G. Mistura, G. Paolicelli, E. Tosatti, A. Vanossi, Adv. Phys. X **2**, 569 (2017)
26. M.Y. Zakhharov, D. Demidov, D.L. Shepelyansky, Phys. Rev. B **99**, 155416 (2019)
27. O.V. Zhirov, D.L. Shepelyansky, Europhys. Lett. **103**, 68008 (2013)
28. A.F. Ioffe, *Semiconductor Thermoelements, and Thermoelectric Cooling* (Infosearch Ltd., 1957)

29. A.F. Ioffe, L.S. Stil'bans, Rep. Prog. Phys. **22**, 167 (1959)
30. A. Majumdar, Science **303**, 777 (2004)
31. H.J. Goldsmid, *Introduction to Thermoelectricity* (Springer, Berlin, 2009)
32. N. Li, J. Ren, L. Wang, G. Zhang, P. Hanggi, B. Li, Rev. Mod. Phys. **84**, 1045 (2012)
33. B.G. Levi, Phys. Today **67**, 14 (2014)
34. J. He, T.M. Tritt, Science **357**, eaak9997 (2017)
35. J.P. Heremans, M.S. Dresselhaus, L.E. Bell, D.T. Morelli, Nat. Nanotechnol. **8**, 471 (2013)
36. S. Bang, D. Wee, A. Li, M. Fornari, B. Kozinsky, J. Appl. Phys. **119**, 205102 (2016)
37. R.L. Gonzalez-Romeo, A. Antonelli, J.J. Melendez, Phys. Chem. Chem. Phys. **19**, 12804 (2017)
38. D.G. Rees, S.-S. Yeh, B.-C. Lee, K. Kono, J.-J. Lin, Phys. Rev. B **96**, 205438 (2017)
39. J.-Y. Lin, A.V. Smorodin, A.O. Badrutdinov, D. Konstantinov, J. Low Temp. Phys. **195**, 1573 (2018)
40. T. Brazda, A. Silva, N. Manini, A. Vanossi, R. Guerra, E. Tosatti, C. Bechinger, Phys. Rev. X **8**, 011050 (2018)
41. S. Lepri, R. Livi, A. Politi, Phys. Rep. **377**, 1 (2003)
42. O.V. Zhirov, D.L. Shepelyansky, Eur. Phys. J. B **82**, 63 (2011)
43. D. Shepelyansky, Scholarpedia **4**, 8567 (2009)
44. Y. Machida, X. Lin, W. Kang, K. Izawa, K. Behnia, Phys. Rev. Lett. **116**, 087003 (2016)
45. V. Narayan, M. Pepper, J. Griffiths, H. Beere, F. Sfigakis, G. Jones, D. Ritchie, A. Ghosh, Phys. Rev. B **86**, 125406 (2012)
46. E. Shimshoni, G. Morigi, S. Fishman, Phys. Rev. Lett. **106**, 010401 (2011)
47. J.C.N. Carvalho, W.P. Ferreira, G.A. Farias, F.M. Peeters, Phys. Rev. B **83**, 094109 (2011)
48. M. Ramm, T. Pruttivarasin, H. Haffner, New J. Phys. **16**, 063062 (2014)
49. N. Freitas, E.A. Martinez, J.P. Paz, Phys. Scr. **91**, 013007 (2016)
50. R.S. Lous, I. Fritsche, M. Jag, B. Huang, R. Grimm, Phys. Rev. A **95**, 053627 (2017)